



Technical note: sea salt interference with black carbon quantification in snow samples using the single particle soot photometer

5 Marco Zanatta^{1,a}, Andreas Herber¹, Zsófia Jurányi¹, Oliver Eppers^{2,3}, Johannes Schneider², Joshua P. Schwarz⁴

¹ Alfred-Wegener-Institut, Helmholtz-Zentrum für Polar- und Meeresforschung (AWI), Bremerhaven, Germany

² Particle Chemistry Department, Max Planck Institute for Chemistry, Mainz, Germany

10 ³Johannes Gutenberg University of Mainz, Institute for Atmospheric Physics, Mainz, Germany

⁴Chemical Sciences Laboratory, Earth System Research Laboratories, Boulder, CO, USA

^anow at LISA, UMR CNRS 7583, Université Paris-Est-Créteil, Université de Paris, Institut Pierre Simon Laplace (IPSL), Créteil, France

15

Correspondence to: Andreas Herber (andreas.herber@awi.de)

Abstract

20 After deposition from the atmosphere, black carbon aerosol (BC) takes part in the snow albedo feedback contributing to modification of the Arctic radiative budget. With the initial goal of quantifying the concentration of BC in the Arctic snow and subsequent climatic impacts, snow samples were collected during the Polarstern expedition PASCAL (Polarstern cruise 106) in the sea ice covered Fram Strait in early summer 2017. The content of refractory BC (rBC) was then quantified in the laboratory of the Alfred
25 Wegener Institute with the single particles soot photometer (SP2). We found strong correlations between both rBC mass concentration and rBC diameter with snow salinity. Therefore, we formulated the hypothesis of a salt-induced matrix effect interfering with the SP2 analysis. By replicating realistic salinity conditions, laboratory experiments indicated a dramatic six-fold reduction in observed rBC concentration with increasing salinity. In the salinity conditions tested in the present work (salt concentration below 0.4
30 g l⁻¹) the impact of salt on nebulization of water droplets might be negligible. However, the SP2 mass detection efficiency systematically decreased with salinity, with the smaller rBC particles being preferentially undetected. The high concentration of suspended salt particles and the formation of thick salt coating on rBC cores might have caused problems to the SP2 analog-to-digital conversion of the signal and incandescence quenching, respectively. Changes to signal acquisition parameters and laser
35 power of the SP2 improved the mass detection efficiency, which, nonetheless, never attained unity values. The present work provides the evidence that high concentration of sea salt undermines the quantification of rBC in snow performed with the SP2. This interference was never reported and might affect future



analysis of rBC particles in snow collected, especially, over sea ice or coastal regions strongly affected by sea salt deposition.

40

1 Introduction

Black carbon aerosol (BC), produced by incomplete combustion of biomass and fossil fuels, is transported from mid-latitude source regions to the Arctic atmosphere (Schacht et al., 2019), where it influences the regional climate (Quinn et al., 2015). Once removed from the atmosphere, BC particles continue to affect the Arctic radiative budget by directly decreasing the snow albedo (Dou and Xiao, 2016) and promoting snow grain growth (Skiles and Painter, 2017). In turn, the acceleration of the melting rate leads to earlier exposure of underlying surface. The overall process is usually called “snow albedo feedback”, and might be considered among the strongest forcing mechanisms in the Arctic region (Hansen and Nazarenko, 2004; Flanner et al., 2007; Skiles et al., 2018).

50 Considering the climatic repercussions caused by BC in snow, the scientific community has been measuring the content of BC in snow across the Arctic for almost four decades (Clarke and Noone, 1985; Doherty et al., 2010; Dou and Xiao, 2016; Tørseth, 2019). Unfortunately, a standardized and universally accepted analytical technique does not yet exist. Generally, the wide variety of analytical approaches to measure BC in snow can be divided in offline and online methods. Considering the offline approach, BC mass can be measured after melting and filtration of the snow sample via thermal-optical analysis (Hagler et al., 2007) or transmittance spectroscopy (Doherty et al., 2010). Alternatively, BC mass might be quantified, after the nebulization of the melted snow samples, with online techniques such as the photoacoustic technique (Schnaiter et al., 2019) or laser induced incandescence technique (Schwarz et al., 2012).

60 In the recent years the laser induced incandescence technique, more specifically the single particle soot photometer (SP2; Droplet Measurement Technologies, Longmont, CO, USA), was often deployed to quantify refractory black carbon particles (rBC; Petzold et al., 2013) in snow in various regions of the Arctic (Khan et al., 2017; Macdonald et al., 2017; Jacobi et al., 2019; Mori et al., 2019; Zhang et al., 2020). The rBC analytical procedure now generally includes three steps: 1) melting of the snow sample, 65 2) nebulization with pneumatic concentric nebulizer equipped with warming-cooling desolvating system (i.e. Marin-5 produced by Teledyne Technologies, Omaha, USA and APEX-Q produced by Elemental Scientific Inc., Omaha, USA), 3) sampling with the SP2. During nebulization, the melted sample is usually transported to the nebulizer at a constant flow rate via a peristaltic pump. The liquid is then broken into small droplets and suspended in a nebulization chamber by means of a pneumatic concentric nebulizer. Once suspended, the solvent in the droplets is evaporated and removed with a warming cooling cycle. Several studies addressed the issue of reducing the losses of rBC during the nebulization phases by controlling liquid flow rate, gas flow rate and pressure and temperature cycle (Lim et al., 2014; Wendl et al., 2014; Mori et al., 2016; Katich et al., 2017). Overall, up to 75% of rBC mass is suspended from the sample, transported through the nebulizer and finally detected by the SP2 without the addition of 75 surfactants (Lim et al., 2014; Mori et al., 2016). Due to reduction of water density and viscosity, the doping with isopropyl alcohol increases the rBC mass nebulization efficiency to values close to unity



(Katich et al., 2017). It must be considered that, despite corrections for the nebulization efficiency, the degree of comparability with more traditional techniques (e.g. thermal-optical method) is still variable (Lim et al., 2014).

80 In the Arctic region, many snow samples were collected in coastal regions and over sea ice (Tørseth, 2019) where the sea salt components often dominate the snow chemical composition, especially in summer in presence of open waters (Krnavek et al., 2012; Jacobi et al., 2019). This is particularly relevant over sea ice, where sea salt aerosol, suspended as sea spray, can be deposited at the snow surface, while capillary upward migration of sea salt from the sea ice can lead to high salt concentration at the bottom
85 of the snowpack (Domine et al., 2004). It turned out that our surface snow samples, collected over the sea ice covered Fram Strait in summer 2017 within the PASCAL experiment, were highly affected by salt deposition, showing a wide range of salinity. The presence of salt might influence the nebulization of the sample, the analyte and solvent transport and even the analytical signal of certain analytical techniques such as inductively coupled plasma atomic emission spectroscopy (e.g. L. Sharp, 1988; Luis Todoli et al.,
90 2002; Burgener and Makonnen, 2020). This effect is commonly called “matrix effect”. At the present time, the potential interference of sea salt during the analysis of rBC particles with the SP2 is not yet assessed.

Considering the high salinity of the snow samples, collected in the Fram Strait, a series of laboratory experiments were conducted to quantify the impact of sea salt on nebulization and rBC detection with the
95 SP2 instrument. This work aims to identify the importance of the salt matrix effect especially in the perspective of the MOSAiC (Multidisciplinary drifting Observatory for the Study of Arctic Climate, <https://mosaic-expedition.org/>) project, where hundreds of snow samples were collected, during the one-year long drift over the sea ice, for the analysis of rBC in snow with the SP2.

2 Technique

100 2.1 Snow sampling during the PASCAL expedition

The PASCAL expedition (Physical Feedbacks of Arctic Boundary Layer, Sea Ice, Cloud and Aerosol; Flores and Macke, 2018), organized within the framework of the AC3 project (Arctic Amplification: Climate Relevant Atmospheric and Surface Processes, and Feedback Mechanisms; Wendisch et al., 2018), was a shipborne field campaign on board of the *RV Polarstern*, the research icebreaker of the
105 Alfred Wegener Institute (Bremerhaven, Germany). The 25 surface snow samples discussed here were collected on the sea ice during the drift phase, which occurred between 3 June and 16 June 2017 in the Fram Strait between 10.0°E - 11.5°E and 81.7°N - 82°N at a distance from open leads between 0.5 km and 1 km. These samples were collected in the first 5 cm of the snow pack and stored frozen at -20°C in polypropylene tubes (Fisher Scientific GmbH, Schwerte, Germany) of 50 ml volume (typically 20-30 g
110 water content) until analysis. For each snow sample physical properties of the corresponding snow layer were also measured. The specific surface area (SSA) was measured with the IceCube instrument (A2 Photonic Sensors, Grenoble, France), the snow density with a custom-made density cutter and the snow temperature with a negative temperature coefficient one channel thermometer (model 101, Testo Ltd, Alton Hampshire, United Kingdom).



115 2.2 Instrumental setup during laboratory analysis

The deployed experimental setup for snow sample analysis is schematized in Figure 1. First, the snow samples were melted in a thermostatic bath at 25°C temperature. Immediately after melting, the electrical conductivity (κ) of the liquid sample was measured with a portable conductivity meter (model: Cond 3110, WTW, Xylem Analytics, Weilheim, Germany) equipped with a 2-electrode conductivity cell (LR 120 325/01). The probe was immersed in the sample and was rinsed with milliQ water before and after each measurement. Since κ increases with the concentration of ions in a solution

The sample was then pumped by a peristaltic pump through a liquid flow meter (model: Liquid Flow Meter SLI, Sensirion AG, Staefa, Switzerland) towards the Marin-5 nebulizer (Teledyne Technologies, Omaha, USA). In the Marin-5, the liquid sample is aerosolized by a concentric pneumatic nebulizer, such that the produced droplets are desolvated by a heating-cooling cycle (110°C-5°C). Finally, the dry aerosol (relative humidity below 30%; Katich et al., 2017) was pumped to the aerosol measuring instruments. More detailed description of the Marine-5 nebulizer can be found in Mori et al. (2016). The liquid (70 $\mu\text{l min}^{-1}$) and air (1 l min^{-1}) flow rates were selected to maximize the suspension of rBC mass following Katich et al. (2017) and kept constant during all experiments. No surfactants were added to the snow 130 samples nor to the test suspensions/solutions. In this work, the aerosolized particles were directed to a Single Particle Soot Photometer (SP2; DMT, Longmont, USA), a Scanning Mobility Particle Sizer (SMPS; TSI; Shoreview, USA) and to the single-particle mass spectrometer ALABAMA (Aircraft-based Laser Ablation Aerosol Mass Spectrometer; Brands et al., 2011; Köllner et al., 2017; Clemen et al., 2020). Our SP2 sampled the aerosol directly from the Marin-5 exhaust and provided number concentration 135 (N_{rBC}), mass concentration (M_{rBC}) and size distribution of rBC in the mass equivalent diameter (D_{rBC}) range of 70-1000 nm. The operation principle of the SP2 for atmospheric applications are given by Stephens et al. (2003), while a complete assessment on the performance of the SP2 during snow sample analysis can be found in Lim et al., (2014), Mori et al. (2016) and Katich et al. (2017). The incandescence detectors of the SP2 were calibrated with mass-selected fullerene soot (FS; Alfa Aesar, LOT: W08A039) 140 as described in Laborde et al. (2012b). The SMPS measured the number concentration (N) and size distribution between 14 nm and 680 nm mobility diameter (D_p). Additionally, the ALABAMA was used to get additional information on the chemical composition of single particles with diameters between approximately 110 and 5000 nm (Clemen et al., 2020). Different chemical species were identified using characteristic marker ions of the mass spectra. Both the SMPS and ALABAMA sampling line included a 145 factor 10 dilution. The transport losses of aerosol particles in the 15-1000 nm particle diameter range were estimated for the SP2 sampling line (0.30 m from the MARIN-5 exhaust), and for the ALABAMA-SMPS sampling line (1 m from the MARIN-5 exhaust). In general, the transport losses for both lines were negligible (<3%) for particles in the 30-1000 nm diameter range, while slightly higher losses (below 7%) were calculated for particles smaller than 30 nm. Considering the similarity of loss 150 between the two sampling lines (SP2 and ALABAMA-SMPS) the transport losses are not considered in the rest of the present work.

2.3 Surface snow properties in the Fram Strait

2.3.1 Snow physical properties



155 Warm conditions were encountered during the drift, with the air temperature increasing from
approximately -4°C at the beginning of the campaign to approximately -1°C (with one-minute average
values up to 2°C) at the end of the drift. As a consequence
of temperature increase, the specific surface area (SSA) decreased from $70\text{ m}^2\text{ kg}^{-1}$ to $5\text{ m}^2\text{ kg}^{-1}$ and snow
density increased from 280 kg m^{-3} to 350 kg m^{-3} . The electrical conductivity of surface snow decreased
160 from values above $1000\text{ }\mu\text{S cm}^{-1}$ to κ values below $10\text{ }\mu\text{S cm}^{-1}$ towards the end of the campaign. The
decrease of SSA and increase of snow density during the drift phase of the PASCAL expedition indicates
the occurrence of melt-refreeze cycles (Haas et al., 2001; Massom et al., 2001; Domine et al., 2007), and
the downward migration of soluble salts with percolating water explains the decrease of κ (Domine et al.,
2004; Doherty et al., 2013). Considering the wide variability of electrical conductivity, the dataset was
165 organized in 5 salinity classes (S_n). The samples with the lowest conductivity ($\kappa \approx 5\text{--}10\text{ }\mu\text{S cm}^{-1}$)
accounted for 38% of total samples and were mainly collected after the melting onset and grouped into
S1. S2 includes the samples collected at the snow melt which showed κ values between approximately
 $20\text{--}30\text{ }\mu\text{S cm}^{-1}$ and accounted for 17% of the samples. The samples characterized by a κ value above $200\text{ }\mu\text{S cm}^{-1}$
and below $2000\text{ }\mu\text{S cm}^{-1}$ represented the 46% of the total number of the collected probes and
170 were organized into three different salinity classes (S3, S4 and S5). The most saline snow sample ($\kappa =$
 $3600\text{ }\mu\text{S cm}^{-1}$) was excluded from further analysis. The mean and boundaries of κ values defining the five
salinity classes are listed Table 1.

2.3.2 Relationship between salinity of snow samples and particle aerosolization

175 In this part of the work we investigate the potential relationship between electrical conductivity, which is
used here as a proxy for salinity, and the properties of aerosolized particles. Note that both N and N_{BC}
presented in this section are not corrected for the nebulization efficiency of the Marin-5 nebulizer.
Under fixed nebulization conditions (constant liquid sample flow and gas flow), a large number of
particles (droplet residues) were suspended by the nebulization process. N increased with the electrical
conductivity of the sample from $6.1 \cdot 10^5\text{ cm}^{-3}$ in low conductivity samples ($\kappa < 10\text{ }\mu\text{S cm}^{-1}$) to $1.5 \cdot 10^6\text{ cm}^{-3}$
180 for samples showing conductivity values above $1000\text{ }\mu\text{S cm}^{-1}$ (Figure 2, Table 1). Similar trend was
recently observed by Rösch and Cziczo (2020). The correlation of N with κ suggest that most of the
aerosolized particles might be composed by sea salt, which is expected to be the major solute in the sea
water. As indicated in Table 1, the size of the aerosolized particles (geometric mean of the number size
distribution; GD_p) increased with κ from 27 nm (S1, $\kappa < 10\text{ }\mu\text{S cm}^{-1}$) to 89 nm (S5, $\kappa > 1000\text{ }\mu\text{S cm}^{-1}$).
185 The $GD_p - \kappa$ relationship and absence of multiple modes in the aerosol size distribution (Figure S1)
supports the assumption of sea salt controlling the aerosol composition. The increase of particle diameter
with liquid concentration of soluble inorganic salts was already observed (Clifford et al., 1993) and found
to be mainly caused by the higher concentration of salt in the primary aerosolized droplets. Next to it,
particle growth caused by coalescence and promoted by the high number concentration of aerosolized
190 particles might also contribute to the diameter shift (Olivares and Houk, 1986). The shift of the size
distribution mode into the size detection range of the SMPS might also contribute to the N - κ positive
correlation shown in Figure 2.

The ALABAMA measurements confirmed the predominant presence of sea water components such as
sodium chloride (NaCl) and magnesium (Mg) over other chemical species shown in Figure 3. The particle



195 fraction (PF) of NaCl-containing particles increased from roughly 30 % for the lowest salinity class to
60-80 % of all analyzed particles for S2, S3, S4 and S5. Similar increase was observed for Mg-containing
particles. Other particle species, e.g. non-sea-salt (nss) nitrate and sulfate, were only abundant in samples
with low conductivity. For salinity class S4, the fraction of NaCl- and Mg-containing particles is
200 significantly lower compared to other classes with $\kappa > 10 \mu\text{S cm}^{-1}$ which is due to one sample of S4
containing more of the other particle species.
SP2 measurements indicated a monotonic decrease of N_{rBC} with conductivity (Figure 2, Table 1), opposite
to N . Considering the salinity classes, the rBC number concentration decreased from approximately 70
 cm^{-3} in S1 to 1.7 cm^{-3} in S5. Additionally, the number size distribution of detected rBC particles showed
a shift to larger diameter as function of salinity (Figure S1). The resulting rBC geometric mean diameter
205 (GD_{rBC}), calculated from the number size distribution, increased from approximately 90 to 120 nm from
S1 to S5 (Table 1). One major aspect surge from these first results: rBC-containing particles represent the
small minority of the aerosol population nebulized from the snow samples. In fact, the number fraction
of rBC particles (F_{rBC}) decreased with salinity from $1.1 \cdot 10^{-2} \%$ in S1 to $1.1 \cdot 10^{-4} \%$ in S5 (Table 1).
Moreover, elemental carbon (EC-) containing particles were found in less than 1% of all analyzed
210 particles by ALABAMA (Figure 3). Hence, considering the remarkable concentration of total particles
and the minor fraction of rBC particles, bench experiments were designed to reproduce the salinity
conditions of PASCAL snow samples in order to investigate the potential interference mechanisms of salt
on rBC detection by the SP2.

2.4 Reproducing realistic snow samples conditions in laboratory experiments

215 The laboratory experiments aimed to reproduce BC snow concentration representative of generic Arctic
conditions, and the specific salinity conditions representative of PASCAL snow samples. It is important
to note that the salt concentrations explored in the present work do not represent realistic conditions
encountered in continental or mountain regions where sea salt aerosol deposition is not dominant. The
ability of reproducing such conditions and practical limitations are presented as following.

220

2.4.1 Sample preparation

Fullerene soot (FS; Alfa Aesar, LOT: W08A039) was used as proxy for ambient black carbon. FS is a
well characterized standard for SP2 calibration (Gysel et al., 2011; Laborde et al., 2012a) and is
consensually accepted as reference standard for ambient black carbon (Moteki and Kondo, 2010;
225 Baumgardner et al., 2012). Three different inorganic salts were initially chosen to replicate the
conductivity array of the snow samples: sodium chloride (NaCl, Fluka), potassium chloride (KCl, Fluka)
and ammonium sulfate ($(\text{NH}_4)_2\text{SO}_4$, Sigma Aldrich).

The proportionality between conductivity and mass concentration of the salts was first assessed (Figure
S2). All the saline solutions showed a linear relationship between conductivity and mass concentration,
230 with high correlation coefficient ($r^2 > 0.98$). We have chosen the concentration range of the dissolved salt
to be between approximately 3 mg l^{-1} and 870 mg l^{-1} to match the salinity values between the lowest and
the highest boundaries of the S1-S5 classes. As in the case of snow samples, the number concentration of
aerosolized particles (measured by the SMPS in the size range of 14-680 nm) increased with salinity
(Figure 4) from approximately $6 \cdot 10^5 \text{ cm}^{-3}$ at S1 ($\kappa \approx 7 \mu\text{S cm}^{-1}$) to approximately $1.7 \cdot 10^6 \text{ cm}^{-3}$ at S5 ($\kappa \approx$



235 $1450 \mu\text{S cm}^{-1}$). The number concentration of particles produced by nebulization of saline solutions is similar to the snow samples with difference below 10% for the S1-S4 classes and below 15% for S5. The increase of particle diameter with conductivity observed in the snow samples was closely replicated by the saline solutions (Figure 5). The increase of concentration and diameter of total suspended particles with salinity observed in the snow samples was successfully reproduced with salt standards, indicating
240 that the use of inorganic salts to simulate the snow saline conditions was justified. Due to the similarity of results between the different salts, and to the fact that NaCl was the major component of PASCAL samples (Figure 3), NaCl was chosen as the reference salt for all the experiments presented in the rest of the study.

245 **2.4.2 Salt induced limitations to SP2 operation**

Although ambient salinity conditions were successfully reproduced, salt presence affected the operation of the SP2. Hence, the BC and salt concentration range was limited, compared to ambient conditions, in order to ensure a correct SP2 analysis.

250 **2.4.2.1 SP2 laser beam shadowing**

During the snow-sample analysis, the large light extinction of the dense aerosol produced from one extremely saline sample ($\kappa = 3600 \mu\text{S cm}^{-1}$) caused a marked but temporary decrease of the YAG power (approximately 50% reduction). The laser power completely and immediately recovered after switching to clean air sampling. Despite this extreme event, in the salinity range of our snow samples ($\kappa < 1652 \mu\text{S cm}^{-1}$), the YAG power showed only a 2% decrease with increasing salinity. This effect on net laser
255 intensity in the cavity might, thus, be important for extremely saline solutions, but negligible for solution or samples with κ below $1500 \mu\text{S cm}^{-1}$ at the rates we nebulized the liquid.

2.4.2.2 SP2 flow system

260 The prolonged sampling of saline solution also affected the flow system of the SP2. First, the continuous injection of high concentration salt particles caused the obstruction of the aerosol jet tubing directing the sampled air into the SP2 detection chamber. The solid salt obstruction could be removed by partial and rapid immersion in water of the jet assembly followed by drying with compressed air. However, this procedure caused a long disruption of the analysis sequence and can alter the jet-laser alignment. The first
265 set of experiments were based on FS suspensions at three mass concentrations: $1 \mu\text{g l}^{-1}$, $5 \mu\text{g l}^{-1}$ and $10 \mu\text{g l}^{-1}$. The clogging frequency was higher at low FS concentration, when the sampling time (needed to acquire minimum of 30 000 recorded particles) was substantially longer than for more FS concentrated suspensions (Figure S3). Although experiments with suspensions at higher FS concentration were less frequently affected by clogging issues the prolonged nebulization (longer than 30 minutes) of saline
270 solutions with electrical conductivity equal and above $800 \mu\text{S cm}^{-1}$ caused systematic clogging of the SP2 aerosol jet tubing. Hereafter, only the results obtained from the nebulization of FS suspension at $10 \mu\text{g l}^{-1}$ will be presented and discussed. This value is fairly representative of central Arctic Ocean snow BC concentration range ($3\text{--}15 \mu\text{g g}^{-1}$) measured with transmittance spectroscopy (Doherty et al., 2010). In order to reduce the clogging occurrence, the upper limit of FS suspension's κ was always set to $800 \mu\text{S cm}^{-1}$ (approximately 0.4 g l^{-1} of NaCl). Considering our inability of reproducing the most extreme sample
275



conditions (low BC and high salt concentration), the SP2 results acquired during the analysis of S5 samples are affected by unknown bias.

280 One also has to pay thorough attention to the particle drying during prolonged saline solution measurements. The transport of the remaining moisture through the SP2 might not directly impact the detection of rBC particles, but it might damage the SP2 pump and inject moist sheath and purge air in the SP2, potentially contaminating the SP2 optics. To avoid this problem, we have installed an additional dryer at the SP2 exhaust and a water trap immediately after the SP2 pump in addition to the standard dryer usually installed between the pump and the SP2 purge-sheath flow.

2.5 Salt impact on the rBC mass quantification by the SP2

285 In this section we investigate the possible impact of salt on the SP2 rBC quantification using the laboratory generated snow sample proxies. When nebulizing liquid samples, the overall mass quantification efficiency of rBC (ϵ) can be calculated as the mass of rBC pumped into the nebulizer per unit time divided by the mass of rBC coming out of the nebulizer in aerosol form and detected by the SP2 per unit time (Katich et al., 2017):

290

$$\epsilon = \frac{M_{\text{rBC-SP2}}}{M_{\text{rBC-smp}}} * \frac{F_{\text{Gas}}}{F_{\text{Liq}}} \quad (1)$$

Where $M_{\text{rBC-SP2}}$ and $M_{\text{rBC-smp}}$ is the mass concentration of rBC particles quantified by the SP2 and the mass concentration of rBC particles in the liquid sample, respectively. F_{Gas} is the gas flow rate applied to nebulizer and F_{Liq} is the liquid flow rate of sample pumped into the nebulizer. The ϵ values obtained for various soot standards suspended in pure water and nebulized with the Marin-5 nebulizer vary between 0.5 and 0.6 (Mori et al., 2016; Katich et al., 2017), while ϵ of 0.75 was calculated by Lim et al. (2014) using a APEX-Q nebulizer. The ϵ calculated in the present work for non-saline FS suspension varied 0.58 and 0.66. These values are in good agreement with the previous studies, indicating a good reproducibility of nebulization conditions during the laboratory experiments. However, the ϵ monotonic decrease of ϵ down to values between 0.33 and 0.21 for the most saline FS suspensions ($\kappa = 800 \text{ cm}^{-1}$) clearly indicated a salt induced bias on the mass quantification efficiency. ϵ may be decomposed in three distinct contributions: the mass nebulization efficiency (ϵ_{Neb}), the transport efficiency (ϵ_{Tm}) and the mass detection efficiency of the SP2 (ϵ_{SP2}). ϵ_{Neb} describes the mass of rBC pumped into the nebulizer per unit time divided by the mass of rBC coming out of the nebulizer in aerosol form per unit time. Hence, ϵ_{Neb} depends on the suspension efficiency of the liquid sample in liquid droplets and on the transport efficiency of the wet and dry aerosol within the nebulizer. ϵ_{Tm} describes the mass of rBC pumped out the nebulizer per unit time divided by the mass of rBC reaching the SP2 sampling inlet per unit time. ϵ_{Tm} is controlled by diffusion and sedimentation losses and depends on flow rate and particle size but also on length and bends of the sampling line. ϵ_{SP2} describes the mass of rBC in aerosol form being introduced to the SP2 laser per unit time divided by the mass of rBC in aerosol form detected by the SP2 per unit of time. Considering typical atmospheric SP2 operation, ϵ_{SP2} was measured to be of 100% in the SP2 size detection range, being independent from the presence of non-absorbing and non-refractory atmospheric components (Schwarz



et al., 2010). It must be considered that past studies always assumed a 100% ε_{SP2} and ε_{Trn} . Therefore, ε (calculated exactly as in this study according to Equation (1)) was usually addressed as nebulization efficiency. The decrease of ε with salinity indicates that, in the presence of salt, this assumption might not be realistic. The potential impact of salt presence on the nebulization and transport efficiency, and on the SP2 detection efficiency will be addressed in the following subsections.

2.5.1 Nebulization and transport efficiency

Inorganic salt can alter water properties such as viscosity and surface tension, modifying the size distribution of droplets produced in the spray chamber and affecting the nebulization efficiency of various analytes (Todolí et al., 2002). High surface tension and viscosity cause an increase of the mean diameter of the liquid droplets suspended by pneumatic nebulizers, decreasing the transport efficiency (L. Sharp, 1988). NaCl concentration above 1 g l^{-1} causes a significant increase of droplet diameter (Clifford et al., 1993) and a decrease of transport efficiency (Sötebier et al., 2016). However, previous studies on pneumatic nebulizers (Dubuisson et al., 1998; Cano et al., 2002) indicated that salt matrix effect on the liquid droplet diameter and transport at concentration below 1 g l^{-1} is negligible. It must be noted that, as summarized by Todolí et al. (2002), several studies have reported different or contradictory results on the impact of matrix effect during nebulization process with pneumatic nebulizers. Thus, the understanding of processes causing diameter increase and efficiency decrease remains uncertain. The viscosity and surface tension of our NaCl solutions was extrapolated from Lide (1995) and Ozdemir et al. (2009), respectively. 0.8 g l^{-1} of NaCl, representative of S5 samples ($\kappa = 1400 \mu\text{S cm}^{-1}$), causes a small increase of both viscosity (+0.08%) and surface tension (+0.03%) compared to pure water. Our calculations and the results of Dubuisson et al. (1998) and Cano et al. (2002) indicate a negligible change of water properties and thus nebulization efficiency for the salinity levels tested in the laboratory experiments (κ below $800 \mu\text{S cm}^{-1}$, NaCl concentration below 0.4 g l^{-1}). Considering the dominant presence of NaCl in the snow samples (Figure 3), our calculations should reflect snow samples conditions. In order to support our calculations, the mass quantification efficiency was calculated for NaCl solutions (ε_{NaCl}) at different salt concentration from SMPS measurements ($14 \text{ nm} < D_p < 680 \text{ nm}$). The aerosolized mass concentration of the NaCl was calculated assuming spherical particles with a density of 2.17 g cm^{-3} . Thanks to the factor 10 dilution, which granted SMPS operation below the highest limit of the detection and low RH (<30%), we assumed a SMPS detection efficiency of 100% in the 14-680 nm diameter range. Thus, ε_{NaCl} should solely be affected by nebulization efficiency. ε_{NaCl} remained very stable (range of 0.57-0.58) from low ($\kappa = 25 \mu\text{S cm}^{-1}$) to high ($\kappa = 800 \mu\text{S cm}^{-1}$) salinity. In turn, this suggest that the nebulization efficiency of rBC particles is independent from salinity (salt concentration below 4 g l^{-1} or electrical conductivity below $800 \mu\text{S cm}^{-1}$). Regarding transport efficiency, diffusion and sedimentation losses during transport, from the nebulizer exhaust to the SP2 (0.3 m of length), were estimated for particles in the SP2 detection range (70-1000 nm) to remains well below 2%; hence not taken into account in forthcoming calculations.

2.5.2 SP2 detection efficiency

In this section we will investigate the consequences of high number particle density transiting the laser beam on the SP2 data acquisition system as function of different acquisition settings. On second instance, the potential quenching of incandescence caused by the formation of thick salt coating on rBC cores will



be addressed. ε_{SP2} is calculated as the ratio between M_{rBC} of the NaCl-doped suspensions at a certain conductivity ($\kappa > 0 \mu\text{S cm}^{-1}$; κ_x) and the M_{rBC} of the non-saline reference suspension ($\kappa \approx 0 \mu\text{S cm}^{-1}$; κ_0) as:

$$\varepsilon_{SP2}(\kappa_x) = \frac{M_{rBC}(\kappa_x)}{M_{rBC}(\kappa_0)} \quad (2)$$

A size dependent ε_{SP2} is defined as the ratio of the mass size distribution at a specific conductivity (κ_x) over the mass size distribution of non-saline suspensions (κ_0) at a certain rBC diameter (D_{rBC}):

$$\varepsilon_{SP2}(\kappa_x, D_{rBC}) = \frac{dM_{rBC}(\kappa_x, D_{rBC})}{dM_{rBC}(\kappa_0, D_{rBC})} \quad (3)$$

where dM_{rBC} represents the mass concentration of rBC particles contained in each individual diameter bin of the rBC mass size distribution.

2.5.2.1 Sensitivity of data acquisition to sample salinity

The frequency of detected scattering events increased up to 17500 counts per second for saline solutions with $250 \mu\text{S cm}^{-1}$ electrical conductivity (Figure S4). Considering the high frequency of concomitant events (multiple particles passing through the laser beam during one acquisition period), this number is most likely underestimated. Operating the SP2 at these overloaded condition might lead to data loss caused by the limitation of the analogue to digital converter and computational power of the instrument's PC. This is possibly responsible for the observed exponential decrease of the frequency of detected scattering events for saline solutions with κ values above $250 \mu\text{S cm}^{-1}$. Concomitant particles and trigger hysteresis (used to reduce some types of data artifacts in the SP2) issues do not only reduce the acquisition of scattering events, but also cause the decrease of detected incandescence events' frequency (Figure S4). Considering the low concentration of rBC particles and high concentration of non-rBC particles, the acquisition settings become extremely important to avoid non-detection of individual incandescence signals. The importance of triggering choices was, hence, tested with $10 \mu\text{g l}^{-1}$ FS concentration and increasing NaCl concentration (conductivity range of $0 - 800 \mu\text{S cm}^{-1}$). The mass detection efficiency was then measured with either the signal acquisition triggering off the high-gain scattering channel ($\varepsilon_{SP2-Tsc}$) or off the broad-band high-gain incandescence channel ($\varepsilon_{SP2-Tin}$).

First, the result obtained by triggering on the scattering detector (the typical setup when operating the SP2 for atmospheric observations) will be discussed. $\varepsilon_{SP2-Tsc}$ steadily decreased with conductivity to 0.34 at $800 \mu\text{S cm}^{-1}$, while the rBC mean diameter increased from 180 at $0 \mu\text{S cm}^{-1}$ nm to 207 nm at $800 \mu\text{S cm}^{-1}$ (Figure 6) The increasing rBC mean diameter suggests the size dependency of $\varepsilon_{SP2-Tsc}$ (see rBC size distribution in Figure S5). $\varepsilon_{SP2-Tsc}$ systematically increased with D_{rBC} across the entire salinity range tested in the present study (Figure 7a). At lower conductivity ($\kappa < 200 \mu\text{S cm}^{-1}$), $\varepsilon_{SP2-Tsc}$ of particles smaller than 100 nm increased from approximately 0.4-0.6 to values above 0.7 for rBC particles larger than 200 nm. The difference of $\varepsilon_{SP2-Tsc}$ across the rBC size distribution was remarkable at higher conductivity ($\kappa > 600 \mu\text{S cm}^{-1}$), where $\varepsilon_{SP2-Tsc}$ increased from 0.1-0.2 for D_{rBC} below 100 nm to 0.4-0.6 for D_{rBC} above 300 nm. It is thus evident that not only the mass, but also the size distribution, of rBC in saline samples might be



390 strongly biased when the standard atmospheric configuration of the SP2 is implemented for snow
measurements with significant salt content. Below $200 \mu\text{S cm}^{-1}$, no significant difference could be
identified between $\epsilon_{\text{SP2-Tsc}}$ and $\epsilon_{\text{SP2-Tin}}$. This result indicates that triggering settings are not crucial for
relatively clean snow samples. Nevertheless, incandescence triggering allowed recovering 20-50% more
rBC mass compared to scattering triggering at higher salinity ($\kappa > 200 \mu\text{S cm}^{-1}$). Similar to $\epsilon_{\text{SP2-Tsc}}$, $\epsilon_{\text{SP2-Tin}}$
395 showed an increasing trend with D_{rBC} at all considered electrical conductivities (Figure 7b). We have to
note here that for D_{rBC} larger than 400 nm the number of the detected rBC particles in the last bins of the
size distribution was extremely low, therefore the statistical uncertainty caused unrealistic ϵ_{SP2} values
above 1. Considering the results presented here, triggering setting does not appear to substantially modify
the size dependency of the SP2 detection efficiency. Nevertheless, scattering trigger should be avoided in
future studies when analyzing rBC in snow samples. Diluting these saline samples to achieve only single
400 particles per detection in the SP2 (Katich et al., 2017), would likely reduce detection problem only for
samples with κ above $200 \mu\text{S cm}^{-1}$ (NaCl concentration above 0.1 g l^{-1}).

2.5.2.2 Incandescence quenching

405 In presence of very thick coatings encapsulating rBC cores, the laser beam of the SP2 might not have
enough power to penetrate the coating, warm the rBC core, evaporate the coating and finally trigger
incandescence. This phenomenon will be called incandescence quenching. During nebulization of saline
samples, the salt, contained in each droplet, will remain on the rBC particles with water evaporation and
lead to the formation of rBC cores encapsulated by thick coatings.

410 As rough estimation, we calculated the theoretical coating thickness of spherical rBC particles having a
diameter of 100 nm, 200 nm, 300 nm, 400 nm, 500 nm contained in $8 \mu\text{m}$ droplets as function of salinity.
We assumed the presence of a single rBC particle per droplet, a concentric core-shell geometry and NaCl
density of 2.16 g cm^{-3} . A diameter of $8 \mu\text{m}$ represents the peak of the primary droplet number size
distribution suspended by various concentric pneumatic nebulizers working with a gas flow rate of 1 L
415 min^{-1} and a liquid flow range of $11\text{-}20 \mu\text{L min}^{-1}$ (Burgener and Makonnen, 2020). The calculated coating
thickness assumptions can be found in Table S2. The thickest coatings are expected for the smallest rBC
cores (100 nm of diameter) with values increasing from 59 nm at $50 \mu\text{S cm}^{-1}$ to 197 nm at $800 \mu\text{S cm}^{-1}$.
Coating thickness for the largest cores considered here (500 nm) were significantly smaller, having values
below 55 nm for most of the considered NaCl concentration. This calculation shows that incandescence
420 quenching would have a stronger influence on the detection of smaller rBC particles. This phenomenon
could explain the measured ϵ_{SP2} values' diameter dependence shown in Figure 7. The calculated coating
thickness is only a rough assumption, since its value strongly depends on the size of the nebulized
droplets. Assuming $12 \mu\text{m}$ and $5 \mu\text{m}$ droplet diameter (upper and lower mode of the size distribution
shown in Burgener and Makonnen, 2020) will increase and decrease the coating thickness value by
425 approximately a factor 2, respectively (Table S1). Laboratory experiments showed that relatively thin
coatings (coating-rBC mass ratio below 3.5) do not have any significant negative impact on the SP2
detection efficiency (Schwarz et al., 2010). According to the coating calculation presented above (droplet
diameter $8 \mu\text{m}$), coating-rBC mass ratio above 3.5 are expected for rBC particles with diameter below
 300 nm . For 100 nm particles, coating-rBC mass ratio were calculated to exceed a value of 7 already at



430 $50 \mu\text{S cm}^{-1}$. Considering our calculation, and results obtained by Schwarz et al. (2010), incandescence quenching might be particularly important for the smallest rBC particles.

To further investigate the potential quenching effect of salt, FS suspension (FS concentration of $10 \mu\text{g l}^{-1}$) with increasing NaCl concentration was additionally nebulized and analyzed with the SP2 operating at maximum YAG-laser power and signal acquisition triggered on the incandescence signal. High YAG-laser power is expected to vaporize thicker coatings and to increase the mass detection efficiency of rBC (Schwarz et al., 2010). During standard operational conditions and for the above presented results, the pump laser was operated with a current of 2800 mA. For the following experiments, the pump-laser current was increased to its upper limit (3200 mA), leading to an increase of the YAG-laser power output from 5.2 V to 6 V. The mass detection efficiency and its size distribution, here called $\varepsilon_{\text{SP2-Ymax}}$, were calculated according to Equation 1 and Equation 2, respectively. $\varepsilon_{\text{SP2-Ymax}}$ decreased monotonically from 0.83 at $50 \mu\text{S cm}^{-1}$ to 0.55 at $800 \mu\text{S cm}^{-1}$ (Figure 6). Although the negative correlation between ε_{SP2} and κ was still present, $\varepsilon_{\text{SP2-Ymax}}$ was systematically (10% on average) higher than $\varepsilon_{\text{SP2-Tin}}$ across the full salinity range ($\kappa > 0 \mu\text{S cm}^{-1}$). If we look at the size dependent efficiency in Figure 7c, we see that the higher laser power did not improve the detection efficiency in the 70-100 nm D_{rBC} range. An improvement of $\varepsilon_{\text{SP2-Ymax}}$ were observed for rBC particles with D_{rBC} larger than 100-150 nm compared $\varepsilon_{\text{SP2-Tin}}$. It is evident that operating the pump laser at the maximum performance we could achieve does not impact the overall decreasing trend of ε_{SP2} with κ , and does not ensure homogeneous size detection of rBC particles. These results are consistent with quenching of incandescence due to coatings, with stronger reductions in smaller and more thickly-coated rBC cores. Diluting these samples to electrical conductivity values below $50 \mu\text{S cm}^{-1}$ (salt concentration of 0.03 g l^{-1}), when ε_{SP2} is higher than 80%, might significantly reduce incandescence quenching. However, dilution factor will linearly increase with conductivity up to a factor 16 for very saline samples ($\kappa = 800 \mu\text{S cm}^{-1}$). Considering the low BC concentration generally observed in Arctic snow, dilution will strongly increase analysis time.

3 Conclusions

455 Laboratory experiments were conducted to assess the interference caused by inorganic salt with SP2 measurements applied to the quantification of rBC mass in saline snow samples. These experiments were designed to reproduce the salinity conditions of snow samples collected over the sea ice covered Fram Strait in summer 2017 during the PASCAL drift shipborne campaign. These salt concentrations might be exclusively encountered in snow collected in coastal areas or over sea ice in vicinity of open water. The total mass quantification efficiency (ε), which consists of the MARIN-5 nebulization efficiency (ε_{Neb}) and the SP2 detection efficiency (ε_{SP2}), was strongly influenced by the salinity of fullerene suspension. Compared to ε of 0.58-0.66 for non-saline fullerene soot suspension, high salinity (electrical conductivity of $800 \mu\text{S cm}^{-1}$ and NaCl concentration of 0.4 g l^{-1}) caused ε drop to 0.2-0.3 in laboratory testing. Considering that the slight increase of density and viscosity of water and the stable ε of 0.57-0.58 for NaCl solutions, ε_{Neb} could be considered to be independent from salinity below NaCl concentration of 1 g l^{-1} . The sensitivity of ε_{SP2} to different SP2 settings was also tested in order to verify: 1) the impact of high number concentration of non-rBC particles on the SP2 signal acquisition; 2) the incandescence quenching produced by thick coatings. Different SP2 settings were tested, but none of them allowed



470 recovering the entirety of rBC mass, with maximum ε_{SP2} of approximately 0.85 and 0.55 for low- and
high- saline samples; respectively. The SP2 detection efficiency was also found to strongly depend on the
rBC particles' diameter. Overall, rBC particles below 100 nm might be substantially undetected, showing
 ε_{SP2} below 0.2 for the most saline samples (electrical conductivity of $800 \mu\text{S cm}^{-1}$ and NaCl concentration
of 0.4 g l^{-1}) compared to values above 0.6 for rBC particles larger than 200 nm. As a consequence of the
variable detection efficiency, the rBC mass of the PASCAL snow samples is affected by a high degree of
475 uncertainty, and underestimated significantly depending on snow salinity. By operating the SP2 in its
optimal triggering setup and maximum YAG-laser power, the rBC mass in the less saline samples,
collected after melting (electrical conductivity below $50 \mu\text{S cm}^{-1}$) and representing 55% of total probes,
are underestimated by a maximum of 17%. In the most saline samples collected before melting (electrical
conductivity above $800 \mu\text{S cm}^{-1}$ and NaCl concentration above 0.4 g l^{-1}) the rBC mass might be
480 underestimated at least by 45%. Moreover, it is important to note that the nebulization and sampling of
saline samples might have negative impact on the SP2 performance. Extremely saline samples could
cause a temporary drop of the YAG-laser output power, while prolonged sampling of even low salinity
samples could cause the clogging of the SP2 aerosol-spray tubing.

The work demonstrates the influences of sea salt on the performances of the SP2 system during the
485 analysis of snow samples containing notable amount of inorganic salt. We aim to draw attention on a
specific technical analytical issue that was never explicitly addressed beforehand, and that might alter the
analysis of future studies conducted in marine regions. Additional work needs to be performed in order
to minimize the impact of the matrix effect and to address the potential interference of salt on other BC
measuring techniques.

490 **Special issue statement.** This article is part of the special issue “Arctic mixed-phase clouds as studied
during the ALOUD/PASCAL campaigns in the framework of (AC)3 (ACP/AMT/ESSD inter-journal
SI)”. It is not associated with a conference.

495 **Acknowledgements:** We gratefully acknowledge the funding by the Deutsche Forschungsgemeinschaft
(DFG, German Research Foundation)– project ID 268020496 – TRR 172, within the Transregional
Collaborative Research Center “Arctic Amplification: Climate Relevant Atmospheric and Surface
Processes, and Feedback Mechanisms (AC)3”. OE acknowledges funding by the Max Planck Graduate
School (MPGC).

500



References

- Baumgardner, D., Popovicheva, O., Allan, J., Bernardoni, V., Cao, J., Cavalli, F., Cozic, J., Diapouli, E., Eleftheriadis, K., Genberg, P. J., Gonzalez, C., Gysel, M., John, A., Kirchstetter, T. W., Kuhlbusch, T. A. J., Laborde, M., Lack, D., Müller, T., Niessner, R., Petzold, A., Piazzalunga, A., Putaud, J. P., Schwarz, J., Sheridan, P., Subramanian, R., Swietlicki, E., Valli, G., Vecchi, R., and Viana, M.: Soot reference materials for instrument calibration and intercomparisons: a workshop summary with recommendations, *Atmos Meas Tech*, 5, 1869–1887, <https://doi.org/10.5194/amt-5-1869-2012>, 2012.
- Brands, M., Kamphus, M., Böttger, T., Schneider, J., Drewnick, F., Roth, A., Curtius, J., Voigt, C., Borbon, A., Beekmann, M., Bourdon, A., Perrin, T., and Borrmann, S.: Characterization of a Newly Developed Aircraft-Based Laser Ablation Aerosol Mass Spectrometer (ALABAMA) and First Field Deployment in Urban Pollution Plumes over Paris During MEGAPOLI 2009, *Aerosol Sci. Technol.*, 45, 46–64, <https://doi.org/10.1080/02786826.2010.517813>, 2011.
- Burgener, J. A. and Makonnen, Y.: Chapter 2 - Nebulization systems, in: *Sample Introduction Systems in ICPMS and ICPOES*, edited by: Beauchemin, D., Elsevier, Amsterdam, 57–142, <https://doi.org/10.1016/B978-0-444-59482-2.00002-6>, 2020.
- Cano, J. M., Todolí, J. L., Hernandis, V., and Mora, J.: The role of the nebulizer on the sodium interferent effects in inductively coupled plasma atomic emission spectrometry, *J Anal Spectrom*, 17, 57–63, <https://doi.org/10.1039/B105077J>, 2002.
- Clarke, A. D. and Noone, K. J.: Soot in the Arctic snowpack: a cause for perturbations in radiative transfer, *Atmospheric Environ.* 1967, 19, 2045–2053, [https://doi.org/10.1016/0004-6981\(85\)90113-1](https://doi.org/10.1016/0004-6981(85)90113-1), 1985.
- Clemen, H.-C., Schneider, J., Klimach, T., Helleis, F., Köllner, F., Hünig, A., Rubach, F., Mertes, S., Wex, H., Stratmann, F., Welti, A., Kohl, R., Frank, F., and Borrmann, S.: Optimizing the detection, ablation, and ion extraction efficiency of a single-particle laser ablation mass spectrometer for application in environments with low aerosol particle concentrations, *Atmospheric Meas. Tech.*, 13, 5923–5953, <https://doi.org/10.5194/amt-13-5923-2020>, 2020.
- Clifford, R. H., Tan, H., Liu, H., Montaser, A., Zarrin, F., and Keady, P. B.: Particle size measurements in the submicron range by the differential electromobility technique: comparison of aerosols from thermospray, ultrasonic, pneumatic and frit-type nebulizers, *Spectrochim. Acta Part B At. Spectrosc.*, 48, 1221–1235, [https://doi.org/10.1016/0584-8547\(93\)80107-6](https://doi.org/10.1016/0584-8547(93)80107-6), 1993.
- Doherty, S. J., Warren, S. G., Grenfell, T. C., Clarke, A. D., and Brandt, R. E.: Light-absorbing impurities in Arctic snow, *Atmospheric Chem. Phys.*, 10, 11647–11680, <https://doi.org/10.5194/acp-10-11647-2010>, 2010.



- Doherty, S. J., Grenfell, T. C., Forsström, S., Hegg, D. L., Brandt, R. E., and Warren, S. G.: Observed vertical redistribution of black carbon and other insoluble light-absorbing particles in melting snow, *J. Geophys. Res. Atmospheres*, 118, 5553–5569, <https://doi.org/10.1002/jgrd.50235>, 2013.
- Domine, F., Sparapani, R., Ianniello, A., and Beine, H. J.: The origin of sea salt in snow on Arctic sea ice and in coastal regions, *Atmospheric Chem. Phys.*, 4, 2259–2271, <https://doi.org/10.5194/acp-4-2259-2004>, 2004.
- Domine, F., Taillandier, A.-S., and Simpson, W. R.: A parameterization of the specific surface area of seasonal snow for field use and for models of snowpack evolution, *J. Geophys. Res. Earth Surf.*, 112, <https://doi.org/10.1029/2006JF000512>, 2007.
- Dou, T.-F. and Xiao, C.-D.: An overview of black carbon deposition and its radiative forcing over the Arctic, *Adv. Clim. Change Res.*, 7, 115–122, <https://doi.org/10.1016/j.accre.2016.10.003>, 2016.
- Dubuisson, C., Poussel, E., and Mermet, J. M.: Comparison of ionic line-based internal standardization with axially and radially viewed inductively coupled plasma atomic emission spectrometry to compensate for sodium effects on accuracy, *J. Anal. At. Spectrom.*, 13, 1265–1269, <https://doi.org/10.1039/A805424J>, 1998.
- Flanner, M. G., Zender, C. S., Randerson, J. T., and Rasch, P. J.: Present-day climate forcing and response from black carbon in snow, *J. Geophys. Res. Atmospheres*, 112, D11202, <https://doi.org/10.1029/2006JD008003>, 2007.
- Flores, H. and Macke, A.: The Expeditions PS106/1 and 2 of the Research Vessel POLARSTERN to the Arctic Ocean in 2017, Alfred-Wegener-Institut, Helmholtz-Zentrum für Polar- und Meeresforschung, https://doi.org/10.2312/BZPM_0719_2018, 2018.
- Gysel, M., Laborde, M., Olfert, J. S., Subramanian, R., and Gröhn, A. J.: Effective density of Aquadag and fullerene soot black carbon reference materials used for SP2 calibration, *Atmos Meas Tech*, 4, 2851–2858, <https://doi.org/10.5194/amt-4-2851-2011>, 2011.
- Haas, C., Thomas, D. N., and Bareiss, J.: Surface properties and processes of perennial Antarctic sea ice in summer, *J. Glaciol.*, 47, 613–625, <https://doi.org/10.3189/172756501781831864>, 2001.
- Hagler, G. S. W., Bergin, M. H., Smith, E. A., Dibb, J. E., Anderson, C., and Steig, E. J.: Particulate and water-soluble carbon measured in recent snow at Summit, Greenland, *Geophys. Res. Lett.*, 34, <https://doi.org/10.1029/2007GL030110>, 2007.
- Hansen, J. and Nazarenko, L.: Soot climate forcing via snow and ice albedos, *Proc. Natl. Acad. Sci.*, 101, 423–428, <https://doi.org/10.1073/pnas.2237157100>, 2004.



- 565 Jacobi, H.-W., Obleitner, F., Costa, S. D., Ginot, P., Eleftheriadis, K., Aas, W., and Zanatta, M.: Deposition of ionic species and black carbon to the Arctic snowpack: combining snow pit observations with modeling, *Atmospheric Chem. Phys.*, 19, 10361–10377, <https://doi.org/10.5194/acp-19-10361-2019>, 2019.
- 570 Katich, J. M., Perring, A. E., and Schwarz, J. P.: Optimized detection of particulates from liquid samples in the aerosol phase: Focus on black carbon, *Aerosol Sci. Technol.*, 51, 543–553, <https://doi.org/10.1080/02786826.2017.1280597>, 2017.
- Khan, A. L., Dierssen, H., Schwarz, J. P., Schmitt, C., Chlus, A., Hermanson, M., Painter, T. H., and McKnight, D. M.: Impacts of coal dust from an active mine on the spectral reflectance of Arctic surface snow in Svalbard, Norway, *J. Geophys. Res. Atmospheres*, 122, 1767–1778, <https://doi.org/10.1002/2016JD025757>, 2017.
- 575 Köllner, F., Schneider, J., Willis, M. D., Klimach, T., Helleis, F., Bozem, H., Kunkel, D., Hoor, P., Burkart, J., Leaitch, W. R., Aliabadi, A. A., Abbatt, J. P. D., Herber, A. B., and Borrmann, S.: Particulate trimethylamine in the summertime Canadian high Arctic lower troposphere, *Atmospheric Chem. Phys.*, 17, 13747–13766, <https://doi.org/10.5194/acp-17-13747-2017>, 2017.
- 580 Krnavek, L., Simpson, W. R., Carlson, D., Domine, F., Douglas, T. A., and Sturm, M.: The chemical composition of surface snow in the Arctic: Examining marine, terrestrial, and atmospheric influences, *Atmos. Environ.*, 50, 349–359, <https://doi.org/10.1016/j.atmosenv.2011.11.033>, 2012.
- Laborde, M., Mertes, P., Zieger, P., Dommen, J., Baltensperger, U., and Gysel, M.: Sensitivity of the Single Particle Soot Photometer to different black carbon types, *Atmos Meas Tech*, 5, 1031–1043, <https://doi.org/10.5194/amt-5-1031-2012>, 2012a.
- 585 Laborde, M., Schnaiter, M., Linke, C., Saathoff, H., Naumann, K.-H., Möhler, O., Berlenz, S., Wagner, U., Taylor, J. W., Liu, D., Flynn, M., Allan, J. D., Coe, H., Heimerl, K., Dahlkötter, F., Weinzierl, B., Wollny, A. G., Zanatta, M., Cozic, J., Laj, P., Hitzenberger, R., Schwarz, J. P., and Gysel, M.: Single Particle Soot Photometer intercomparison at the AIDA chamber, *Atmospheric Meas. Tech.*, 5, 3077–3097, <https://doi.org/10.5194/amt-5-3077-2012>, 2012b.
- 590 Lide, D. R.: *CRC Handbook of Chemistry and Physics: A Ready-reference Book of Chemical and Physical Data*, CRC Press, 2648 pp., 1995.
- Lim, S., Faïn, X., Zanatta, M., Cozic, J., Jaffrezo, J.-L., Ginot, P., and Laj, P.: Refractory black carbon mass concentrations in snow and ice: method evaluation and inter-comparison with elemental carbon measurement, *Atmos Meas Tech*, 7, 3307–3324, <https://doi.org/10.5194/amt-7-3307-2014>, 2014.
- 595 L. Sharp, B.: Pneumatic nebulisers and spray chambers for inductively coupled plasma spectrometry. A review. Part 1. Nebulisers, *J. Anal. At. Spectrom.*, 3, 613–652, <https://doi.org/10.1039/JA9880300613>, 1988.



- Luis Todolí, J., Gras, L., Hernandis, V., and Mora, J.: Elemental matrix effects in ICP-AES, *J. Anal. At. Spectrom.*, 17, 142–169, <https://doi.org/10.1039/B009570M>, 2002.
- 600 Macdonald, K. M., Sharma, S., Toom, D., Chivulescu, A., Hanna, S., Bertram, A. K., Platt, A., Elsasser, M., Huang, L., Tarasick, D., Chellman, N., McConnell, J. R., Bozem, H., Kunkel, D., Lei, Y. D., Evans, G. J., and Abbatt, J. P. D.: Observations of atmospheric chemical deposition to high Arctic snow, *Atmospheric Chem. Phys.*, 17, 5775–5788, <https://doi.org/10.5194/acp-17-5775-2017>, 2017.
- 605 Massom, R. A., Eicken, H., Hass, C., Jeffries, M. O., Drinkwater, M. R., Sturm, M., Worby, A. P., Wu, X., Lytle, V. I., Ushio, S., Morris, K., Reid, P. A., Warren, S. G., and Allison, I.: Snow on Antarctic sea ice, *Rev. Geophys.*, 39, 413–445, <https://doi.org/10.1029/2000RG000085>, 2001.
- Mori, T., Moteki, N., Ohata, S., Koike, M., Goto-Azuma, K., Miyazaki, Y., and Kondo, Y.: Improved technique for measuring the size distribution of black carbon particles in liquid water, *Aerosol Sci. Technol.*, 50, 242–254, <https://doi.org/10.1080/02786826.2016.1147644>, 2016.
- 610 Mori, T., Goto-Azuma, K., Kondo, Y., Ogawa-Tsukagawa, Y., Miura, K., Hirabayashi, M., Oshima, N., Koike, M., Kupiainen, K., Moteki, N., Ohata, S., Sinha, P. R., Sugiura, K., Aoki, T., Schneebeli, M., Steffen, K., Sato, A., Tsushima, A., Makarov, V., Omiya, S., Sugimoto, A., Takano, S., and Nagatsuka, N.: Black Carbon and Inorganic Aerosols in Arctic Snowpack, *J. Geophys. Res. Atmospheres*, 124, 13325–13356, <https://doi.org/10.1029/2019JD030623>, 2019.
- 615 Moteki, N. and Kondo, Y.: Dependence of Laser-Induced Incandescence on Physical Properties of Black Carbon Aerosols: Measurements and Theoretical Interpretation, *Aerosol Sci. Technol.*, 44, 663–675, <https://doi.org/10.1080/02786826.2010.484450>, 2010.
- Olivares, J. A. and Houk, R. S.: Suppression of analyte signal by various concomitant salts in inductively coupled plasma mass spectrometry, *Anal Chem U. S.*, 58:1, <https://doi.org/10.1021/ac00292a008>, 1986.
- 620 Ozdemir, O., Karakashev, S. I., Nguyen, A. V., and Miller, J. D.: Adsorption and surface tension analysis of concentrated alkali halide brine solutions, *Miner. Eng.*, 22, 263–271, <https://doi.org/10.1016/j.mineng.2008.08.001>, 2009.
- Petzold, A., Ogren, J. A., Fiebig, M., Laj, P., Li, S.-M., Baltensperger, U., Holzer-Popp, T., Kinne, S., Pappalardo, G., Sugimoto, N., Wehrli, C., Wiedensohler, A., and Zhang, X.-Y.: Recommendations for reporting “black carbon” measurements, *Atmos Chem Phys*, 13, 8365–8379, <https://doi.org/10.5194/acp-13-8365-2013>, 2013.
- 625 Quinn, P. K., Stohl, A., Arnold, S., Baklanov, A., Berntsen, T. K., Christensen, J. H., Eckhardt, S., Flanner, M., Klimont, Z., Korsholm, U. S., and others: AMAP Assessment 2015: Black carbon and ozone as Arctic climate forcers, 2015.



- 630 Rösch, M. and Cziczo, D. J.: Aqueous particle generation with a 3D printed nebulizer, *Aerosols/Laboratory Measurement/Instruments and Platforms*, <https://doi.org/10.5194/amt-2020-155>, 2020.
- Schacht, J., Heinold, B., Quaas, J., Backman, J., Cherian, R., Ehrlich, A., Herber, A., Huang, W. T. K., Kondo, Y., Massling, A., Sinha, P. R., Weinzierl, B., Zanatta, M., and Tegen, I.: The importance of the representation of air pollution emissions for the modeled distribution and radiative effects of black carbon in the Arctic, *Atmospheric Chem. Phys.*, 19, 11159–11183, <https://doi.org/10.5194/acp-19-11159-2019>, 2019.
- 635
- Schnaiter, M., Linke, C., Ibrahim, I., Kiselev, A., Waitz, F., Leisner, T., Norra, S., and Rehm, T.: Specifying the light-absorbing properties of aerosol particles in fresh snow samples, collected at the Environmental Research Station Schneefernerhaus (UFS), Zugspitze, *Atmospheric Chem. Phys.*, 19, 10829–10844, <https://doi.org/10.5194/acp-19-10829-2019>, 2019.
- 640
- Schwarz, J. P., Spackman, J. R., Gao, R. S., Perring, A. E., Cross, E., Onasch, T. B., Ahern, A., Wrobel, W., Davidovits, P., Olfert, J., Dubey, M. K., Mazzoleni, C., and Fahey, D. W.: The Detection Efficiency of the Single Particle Soot Photometer, *Aerosol Sci. Technol.*, 44, 612–628, <https://doi.org/10.1080/02786826.2010.481298>, 2010.
- 645
- Schwarz, J. P., Doherty, S. J., Li, F., Ruggiero, S. T., Tanner, C. E., Perring, A. E., Gao, R. S., and Fahey, D. W.: Assessing Single Particle Soot Photometer and Integrating Sphere/Integrating Sandwich Spectrophotometer measurement techniques for quantifying black carbon concentration in snow, *Atmos Meas Tech*, 5, 2581–2592, <https://doi.org/10.5194/amt-5-2581-2012>, 2012.
- 650
- Skiles, S. M. and Painter, T.: Daily evolution in dust and black carbon content, snow grain size, and snow albedo during snowmelt, Rocky Mountains, Colorado, *J. Glaciol.*, 63, 118–132, <https://doi.org/10.1017/jog.2016.125>, 2017.
- Skiles, S. M., Flanner, M., Cook, J. M., Dumont, M., and Painter, T. H.: Radiative forcing by light-absorbing particles in snow, *Nat. Clim. Change*, 8, 964–971, <https://doi.org/10.1038/s41558-018-0296-5>, 2018.
- 655
- Sötebier, C., Kutscher, D., Rottmann, L., Jakubowski, N., Panne, U., and Bettmer, J.: Combination of single particle ICP-QMS and isotope dilution analysis for the determination of size, particle number and number size distribution of silver nanoparticles, *J. Anal. At. Spectrom.*, 31, 2045–2052, <https://doi.org/10.1039/C6JA00137H>, 2016.
- 660
- Tørseth, K.: Review of Observation Capacities and Data Availability for Black Carbon in the Arctic Region: EU Action on Black Carbon in the Arctic – Technical Report 1, 2019.
- Wendisch, M., Macke, A., Ehrlich, A., Lüpkes, C., Mech, M., Chechin, D., Dethloff, K., Velasco, C. B., Bozem, H., Brückner, M., Clemen, H.-C., Crewell, S., Donth, T., Dupuy, R., Ebell, K., Egerer, U.,



- Engelmann, R., Engler, C., Eppers, O., Gehrman, M., Gong, X., Gottschalk, M., Gurbeyre, C.,
665 Griesche, H., Hartmann, J., Hartmann, M., Heinold, B., Herber, A., Herrmann, H., Heygster, G., Hoor,
P., Jafariserajehlou, S., Jäkel, E., Järvinen, E., Jourdan, O., Kästner, U., Kecorius, S., Knudsen, E. M.,
Köllner, F., Kretzschmar, J., Lelli, L., Leroy, D., Maturilli, M., Mei, L., Mertes, S., Mioche, G., Neuber,
R., Nicolaus, M., Nomokonova, T., Notholt, J., Palm, M., van Pinxteren, M., Quaas, J., Richter, P., Ruiz-
Donoso, E., Schäfer, M., Schmieder, K., Schnaiter, M., Schneider, J., Schwarzenböck, A., Seifert, P.,
670 Shupe, M. D., Siebert, H., Spreen, G., Stapf, J., Stratmann, F., Vogl, T., Welti, A., Wex, H., Wiedensohler,
A., Zänata, M., and Zeppenfeld, S.: The Arctic Cloud Puzzle: Using ACLOUD/PASCAL Multiplatform
Observations to Unravel the Role of Clouds and Aerosol Particles in Arctic Amplification, *Bull. Am.
Meteorol. Soc.*, 100, 841–871, <https://doi.org/10.1175/BAMS-D-18-0072.1>, 2018.
- Wendl, I. A., Menking, J. A., Färber, R., Gysel, M., Kaspari, S. D., Laborde, M. J. G., and Schwikowski,
675 M.: Optimized method for black carbon analysis in ice and snow using the Single Particle Soot
Photometer, *Atmos Meas Tech*, 7, 2667–2681, <https://doi.org/10.5194/amt-7-2667-2014>, 2014.
- Zhang, Y., Kang, S., Gao, T., Sprenger, M., Dou, T., Han, W., Zhang, Q., Sun, S., Du, W., Chen, P., Guo,
J., Cui, X., and Sillanpää, M.: Dissolved organic carbon in Alaskan Arctic snow: concentrations, light-
absorption properties, and bioavailability, *Tellus B Chem. Phys. Meteorol.*, 72, 1–19,
680 <https://doi.org/10.1080/16000889.2020.1778968>, 2020.



Tables

685 **Table 1 Properties of snow samples grouped in conductivity classes. Conductivity of melted samples measured between 20 and 25 °C. Mass mixing ratio (M_{rBC}) and geometric mean of the number and mass sized distribution (GD_{rBC}) measured between 60 and 1000 nm of D_{rBC} . Number concentration of the total aerosolized particles (N) measured in the mobility diameter range 14–685 nm. Geometric mean of the total aerosol number size distribution (GD_P). Number fraction of rBC particles (F_{rBC}).**

Salinity class	Fraction sample [%]	Conductivity [$\mu\text{S cm}^{-1}$]			N [cm^{-3}]		N_{rBC} [cm^{-3}]		F_{rBC} [%]	D_P [nm]	D_{rBC} [nm]
		Lower boundary	Upper boundary	Mean	Mean	SD	Mean	SD	Mean	Geometric mean number	Geometric mean number
S1	38	5.3	10.3	7.07	$6.1 \cdot 10^5$	$1.3 \cdot 10^5$	69.6	34.04	$1.1 \cdot 10^{-2}$	27.3	87.6
S2	17	19.6	33.1	24.9	$9.5 \cdot 10^5$	$1.0 \cdot 10^5$	13.1	1.64	$1.4 \cdot 10^{-3}$	34.4	89.2
S3	21	219	343	266	$1.3 \cdot 10^6$	$6.2 \cdot 10^4$	6.81	2.03	$5.2 \cdot 10^{-4}$	57.6	94.2
S4	13	466	533	497	$1.4 \cdot 10^6$	$6.7 \cdot 10^4$	4.45	3.71	$3.1 \cdot 10^{-4}$	72.1	106
S5	13	1275	1652	1424	$1.5 \cdot 10^6$	$9.0 \cdot 10^4$	1.71	0.26	$1.1 \cdot 10^{-4}$	89.0	120

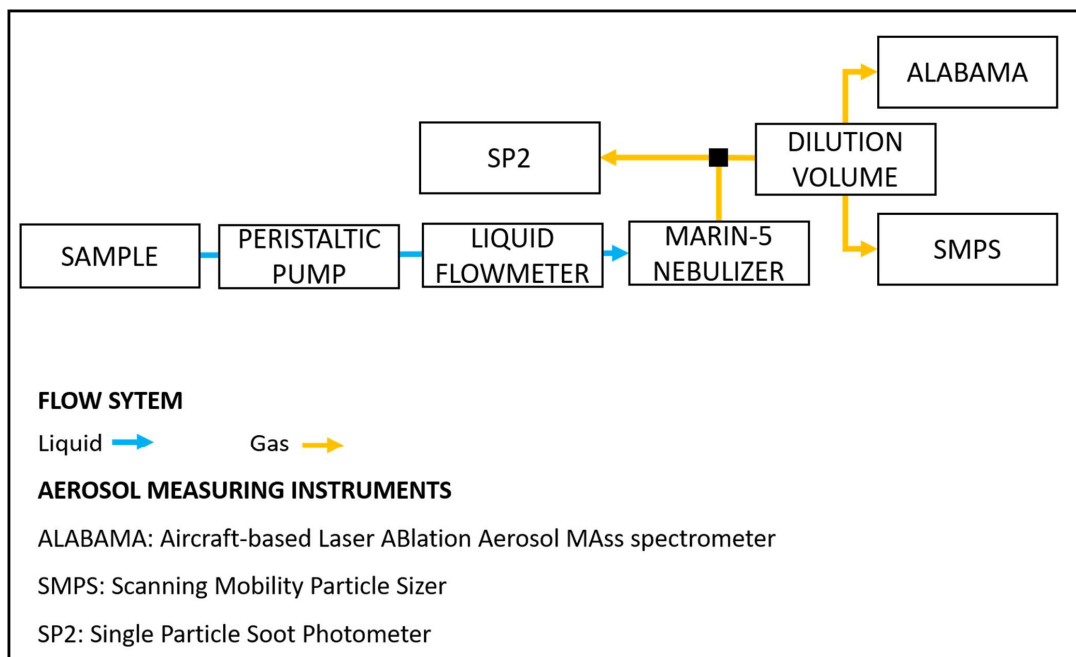
690 **Table 2 Summary of the analysis of fullerene soot suspensions at a concentration of $10 \mu\text{g l}^{-1}$ doped with NaCl for different SP2 settings: Tsc = scattering trigger and standard YAG-laser power, Tsc = scattering trigger and standard YAG-laser power; Tin = incandescence trigger and standard YAG-laser power; Ymax = incandescence trigger and maximum YAG-laser power. SP2 detection efficiency (ϵ_{SP2}), geometric mean of the rBC mass size distribution (GD_{rBC}) listed as function of increasing electrical conductivity (κ) measured between 24 and 25°C.**

κ [$\mu\text{S cm}^{-1}$]	ϵ_{SP2} [-]			GD_{rBC} [nm]		
	Tsc	Tin	Ymax	Tsc	Tin	Ymax
0	1	1	1	183	180	183
50	0.77	0.79	0.83	188	190	191
100	0.74	0.75	0.79	193	192	193
200	0.58	0.57	0.71	195	195	197
400	0.47	0.56	0.61	198	200	204
600	0.41	0.51	0.57	203	206	207
800	0.34	0.5	0.54	206	211	211

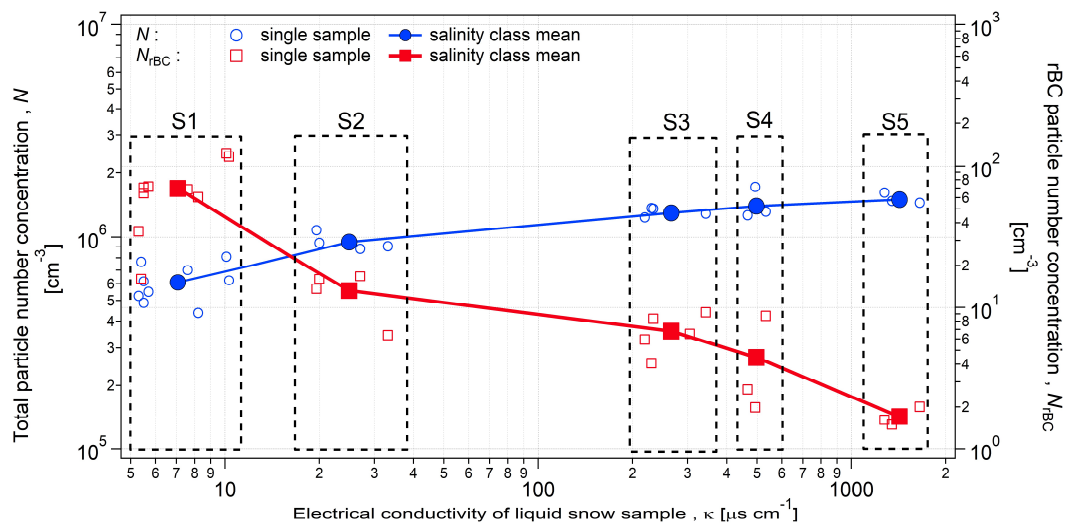
695



700 **Figures**



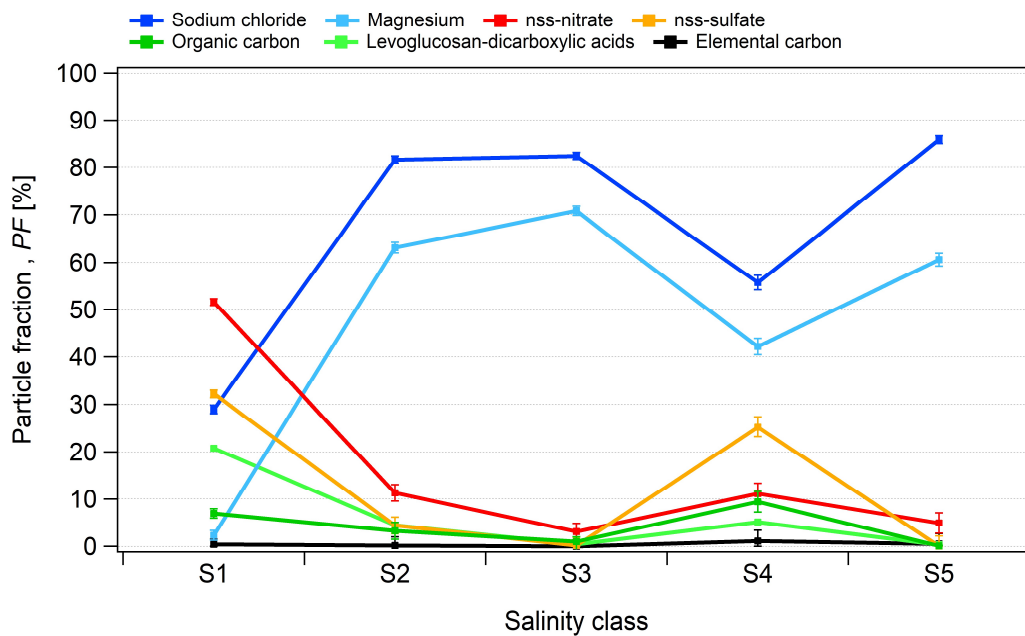
705 **Figure 1** Schematics of the instrumental setup deployed to analyze the PASCAL snow samples and to perform the laboratory test experiments. ALABAMA not available for laboratory test experiments.



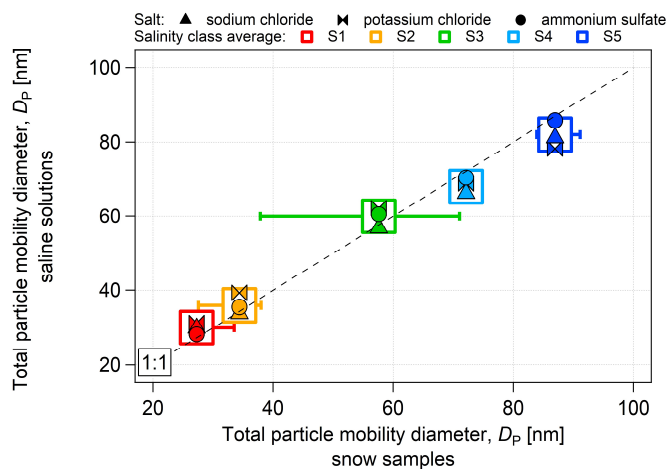
710

Figure 2 Number concentration of the total particles (N) and rBC particles (N_{rBC}) produced from the nebulization of PASCAL snow samples as function of the electrical conductivity of melted snow samples. Boxes indicates the salinity classes (S_n). N measured with the SPMS in the 14-680 nm diameter range nm. N_{rBC} measure with the SP2 in the 70-1000 nm diameter range.

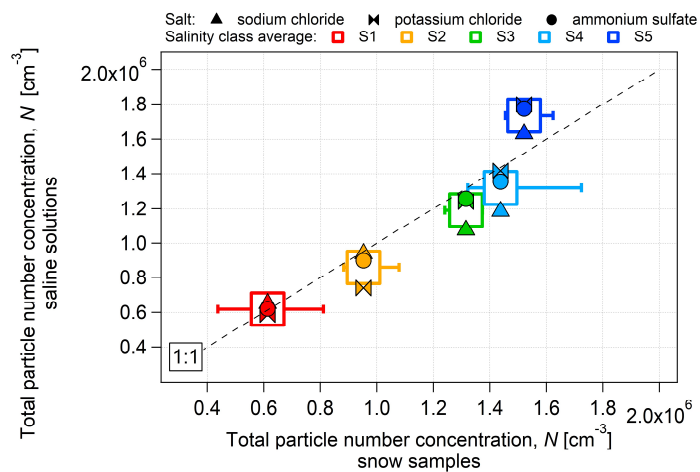
715



720 Figure 3 Number fraction of analyzed particles (*PF*) containing given chemical species measured by ALABAMA in the PASCAL snow samples as a function of the salinity classes (*S_n*). The selected species: sodium chloride (NaCl), non-sea-salt (nss) nitrate, nss sulfate, magnesium (Mg), levoglucosan and dicarboxylic acids, organic carbon (OC) and elemental carbon (EC). Chemical composition measured for particles in the 110-5000 nm diameter range.

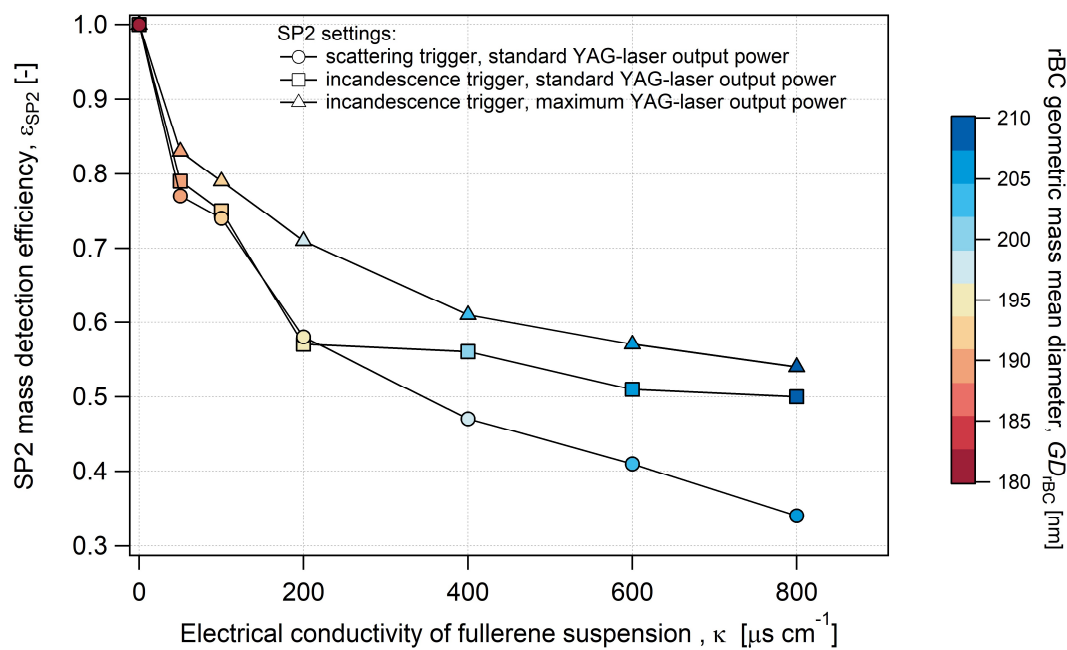


725 **Figure 4** Comparison of number concentration of aerosolized particles produced from inorganic salt solutions (sodium chloride, potassium chloride, ammonium sulfate) and from snow samples as function of salinity.

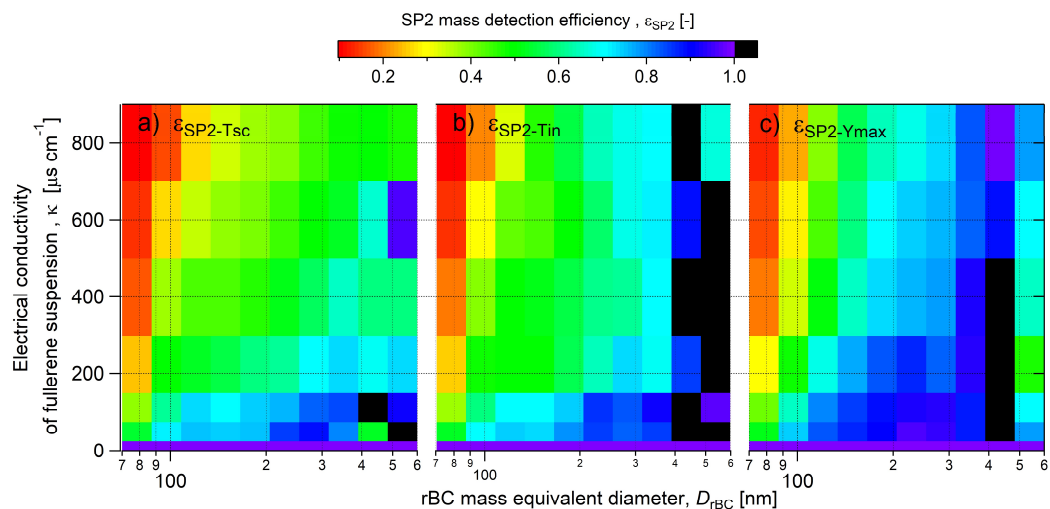


730 **Figure 5** Comparison of diameter of aerosolized particles produced from inorganic salt solutions (sodium chloride, potassium chloride, ammonium sulfate) and from snow samples as function of salinity. Diameter expressed as geometric mean diameter calculated from the number size distribution of aerosolized particles.

735



740 Figure 6 Mass detection efficiency of the SP2 for different SP2 settings and increasing electrical conductivity. Data acquired from the analysis of a fullerene soot suspension at $10 \mu\text{g l}^{-1}$.



745 Figure 7 rBC mass detection efficiency as function of D_{rBC} for different SP2 settings. a) acquisition triggered on the scattering detector with standard YAG-laser output power, $\epsilon_{\text{SP2-Tsc}}$; b) acquisition triggered on the incandescence detector with standard YAG-laser output power $\epsilon_{\text{SP2-Tin}}$; c) acquisition triggered on the incandescence detector with maximum YAG-laser output power, $\epsilon_{\text{SP2-Ymax}}$. Results for fullerene soot suspensions with a concentration of $10 \mu\text{g l}^{-1}$.